

Electronic Supplementary Information

**Highly-Reversible and Recyclable Zinc Metal Batteries Achieved
by Inorganic/organic Hybrid Separator with Finely Tunable
Hydrophilic-Hydrophobic Balance**

Lingbo Yao^{a,b}, Gege Wang^{a,b}, Feifan Zhang^{a,b}, Xiaowei Chi^{a}, Yu Liu^{a*}*

^aShanghai Institute of Ceramics, Chinese Academy of Sciences
Shanghai 200050, China

^bUniversity of Chinese Academy of Sciences
Beijing 100049, China

*Email: xwchi@mail.sic.ac.cn; yuliu@mail.sic.ac.cn

Experimental Section

Materials and Fabrication of P/FS-Z Separators

Raw materials: Fumed silica (FS), ZnO, MgO, ZrO₂, TiO₂, SnO₂, MoO₃, Al₂O₃, Bi₂O₃, Sb₂O₅, and Nb₂O₅ were purchased from Shanghai Aladdin Bio-Chem Technology Co., Ltd. Zinc acetate dihydrate (Zn(Ac)₂·2H₂O), zinc sulfate heptahydrate (ZnSO₄·7H₂O) and manganese sulfate monohydrate (MnSO₄·H₂O) were purchased from Sinopharm Chemical Reagent Co., Ltd, and polytetrafluoroethylene (PTFE) concentrated disperse lotion (60 wt%) was purchased from Shanghai Huayi 3F New Materials Co., Ltd.

P/FS-Z separator: Before fabrication, 0.6 g FS and 2.2 g Zn(Ac)₂·H₂O (grinding and screening using 300 mesh sieve) were pre-dispersed in 10 mL 1 M Zn(Ac)₂ solution (absolute ethanol and water with a volume ratio of 4:1 were used as the solvent). Then 5 g of PTFE dispersion lotion was dropped into the above mixture and the FS-PTFE slurry with Zn(Ac)₂ was ball-milled at 400 rpm min⁻¹ for 4 h to stimulate the homogenization and fibrillation. The dough-like gel product was finally wet-rolled into the desired membrane. Then, the P/FS-Z membrane was stamped into 17 mm diameter membrane as the separator and soaked with the 2 M ZnSO₄ or 2 M ZnSO₄+0.2 M MnSO₄ aqueous electrolyte with a volume of 4 mL for 6 h to dissolve the Zn(Ac)₂ salt and increase the porosity of the separator. The soaking solution was kept for the following cell test. For comparison, pure PTFE membrane without FS, the separators using other fillers, and the separator without Zn(Ac)₂ were also prepared using the same process.

Materials Characterization

The phase structures of Zn foils and separators before and after cycling were identified by X-ray diffraction (XRD, Rigaku Ultima diffractometer with Cu K α radiation, $\lambda = 1.5418 \text{ \AA}$). Scanning electron microscopy (SEM, JEOL, JSM-6510)

equipped with the energy dispersion spectrometer was employed to observe the morphology and elements distribution of the Zn foils and separators. Prior to imaging, the Zn foils and separators were sputtered with gold in vacuum. The tensile strength of the P/FS-Z and commercial GF separators was obtained by a universal material testing machine (Instron-5592) using the standard rectangular tensile specimens (length×width: 20×5 cm², thickness: 300 μm for P/FS-Z and 700 μm for GF). The nanoindentation hardness was characterized on a nanoindentation instrument (Bruker Hysitron TI980). Contact angle measurements of the electrolytes on the separators were performed by a contact angle measurement system (CA100D, Yinnuo). Characteristic functional groups and bond structures were analyzed by the attenuated total reflection Fourier transform infrared spectroscopy (ATR-FTIR, Thermo Scientific Nicolet iS5) in the range of 4000 to 400 cm⁻¹. The number of scans was 32 and the resolution for FTIR measurements was 4 cm⁻¹. The thermal properties and phase contents of P/FS-Z were characterized by a thermogravimetric analyzer (TGA, NETZSC, STA 409 PC) with a heating rate of 5 °C min⁻¹ in the air atmosphere. N₂ was used as the protecting gas. The N₂ adsorption-desorption isotherms of the separators were measured by a gas adsorption analyzer at 77 K, and the pore size distribution of the samples was calculated by the BJH method and DFT method. The electronic structure and corresponding composition were characterized by X-ray photoelectron spectroscopy (XPS, Thermo Scientific K-Alpha). Morphology and roughness of the separators were analyzed by optical profiler (Mahr LD130).

The electrolyte uptake (%) was calculated according to:

$$\text{Electrolyte uptake} = \frac{M - M_0}{M_0} \times 100\%$$

where M_0 and M (average of five tests) are the weight of the separators before and after soaking in the 2 M ZnSO₄ electrolyte for 5 min.

The porosity was calculated according to the equation:

$$\text{porosity} = \frac{W' - W''}{\rho V}$$

where W' and W'' represent the weights of the separator before and after 1 h immersion in n-butyl alcohol, respectively. The ρ and V are the density of the n-butyl alcohol and

volume of the separator, respectively.

Electrodes Preparation and Cells Assembly

δ -MnO₂ was prepared according to our previous study¹. δ -MnO₂, acetylene black and PVDF with a mass ratio of 7:2:1 were mixed to obtain uniform slurry, which was then coated on titanium foil by doctor-blading method and dried overnight at 80 °C. The average MnO₂ loading was 1-2 mg cm⁻². 120 μ m and 10 μ m thick Zn foils were polished to remove the oxide layer. 2 M ZnSO₄ + 0.2 M MnSO₄ (denoted as ZS+MS) or 2 M ZnSO₄ (denoted as ZS) of the separator was configured as the full cell electrolyte or the symmetric cell electrolyte. As mentioned above, the soaking solution was used as the electrolyte when the cell uses the P/FS-Z separator. For the high-capacity pouch cell, the high mass loading cathode was prepared according to our previous work¹. Basically, δ -MnO₂, acetylene black, and PTFE (mass ratio: 7:2:1) were evenly mixed in a mortar, and isopropanol was dropped for demulsification until the mixture was ground into a dough. The mixture was rolled onto a stainless-steel mesh. Before using, it was vacuum-dried and fully soaked in the electrolyte overnight. Three MnO₂ loadings of 10 mg cm⁻², 46.9 mg cm⁻² and 84.9 mg cm⁻² with the negative/positive capacity ratios (N/P) of 11.3:1, 2.12:1 and 1.17:1, respectively, were studied. Zinc foil connected to copper foil with a conductive carbon slurry (AB: PVDF=9:1) was used as the anode. The cathode and the P/FS-Z separator were pre-soaked with aqueous electrolyte and then laminated with Zn anode to achieve the desired pouch cell.

Electrochemical Measurement

Electrochemical impedance spectroscopy (EIS), chronoamperometry (CA), linear sweeping voltammetry (LSV), and cyclic voltammetry (CV) were performed on the electrochemical workstation (CHI 750E). The AC signal ranging from 0.01 Hz to 100 kHz was used for all the EIS tests. Galvanostatic charge/discharge (GCD) cycling tests were carried out on the LAND CT2100A. Tafel tests were conducted using a scanning rate of 1 mV s⁻¹ with Zn working electrode, Zn counter electrode, and saturated calomel

electrode (SCE) as the reference electrode. The bare titanium, Zn foil, and SCE were used as the working, counter, and reference electrodes, respectively, for LSV test with a scanning rate of 1 mV s⁻¹ while separator was attached to the working electrode surface in a test chamber. CV tests were operated using a scanning rate of 0.5 mV s⁻¹.

The transference number of zinc ions ($t_{Zn^{2+}}$) was calculated according to the CA test using the equation:

$$t_{Zn^{2+}} = \frac{I_s(\Delta V - I_0 R_0)}{I_0(\Delta V - I_s R_s)}$$

where I_s and I_0 are the initial and steady-state current, ΔV is the applied constant potential (10 mV), and R_0 and R_s are the initial and steady-state interface resistance.

The Zn^{2+} conductivity of the separators was calculated according to the equation:

$$\sigma_{Zn^{2+}} = \frac{L}{R_b \cdot S} \cdot t_{Zn^{2+}}$$

where L and S are the thickness and area of the electrode, respectively, R_b is the ohmic resistance and M is weight of electrolyte.

The differential capacitance curve was calculated from the equation:

$$C = -(\omega Z_{im})^{-1}$$

where C is the differential capacitance and ω is the angular frequency, Z_{im} is the imaginary part of the impedance, and 1000 Hz was selected as the specific frequency.

In addition, in order to explore the diffusion behavior of Zn||MnO₂ cells using different separators, GITT test was conducted and the diffusion coefficient was calculated based on the equation:

$$D = \frac{4}{\pi\tau} \left(\frac{m_B V_M}{M_B S} \right)^2 \left(\frac{\Delta E_s}{\Delta E_t} \right)^2$$

where m_B , V_M and M_B are the mass, molar volume and molar mass of MnO₂, respectively. τ is the relaxation time, S is the electrode area, ΔE_t is the voltage change caused by charging and discharging (300 s), and ΔE_s is the voltage change caused by pulse (3600 s).

Theoretical Calculations

As previously reported², in the traditional 2 M ZnSO₄ aqueous electrolyte, it is universally acknowledged that six water molecules enter the primary solvated shell of each zinc ion, and accordingly, the corresponding [Zn(H₂O)₆]²⁺ initial solvated structure was constructed. This work focuses on the same solvation structure under the influence of one 3 Å FS cluster. To obtain the optimized structure of [Zn(H₂O)_m]²⁺-FS. All calculations were carried out on ORCA 5.01 package³. B3LYP functional and def2-TZVP(-f) basis sets were used for structural optimization and static single-point energy calculation. In addition, DFT-D3 was introduced to compensate for the accuracy of the basis set in describing the dispersion relationship⁴. At the same time, in order to make the simulation close to the aqueous environment, the implicit solvation model SMD was used to simulate the solvation effect⁵. FT-IR spectra of FS was simulated by Multiwfn program⁶.

The solvation energy of zinc ion in the coordination complex Zn(H₂O)_m²⁺-FS was calculated by the following formula:

$$E_{sol} = E([Zn(H_2O)_m(FS)_n]^{2+}) - E(Zn^{2+}) - mE(H_2O) - E(FS)$$

Where E is the total Gibbs free energy of each unit calculated from DFT; M and n are the numbers of H₂O and FS in the solvated sheath of Zn²⁺ ions, respectively.

The binding energy is calculated based on the following formula:

$$E_{be} = E_{A+B} - (E_A + E_B)$$

Among them, the E_{A+B} is the Gibbs free energy of combination A and B and the second item is the sum of the Gibbs free energy of individual A and B.

Figures

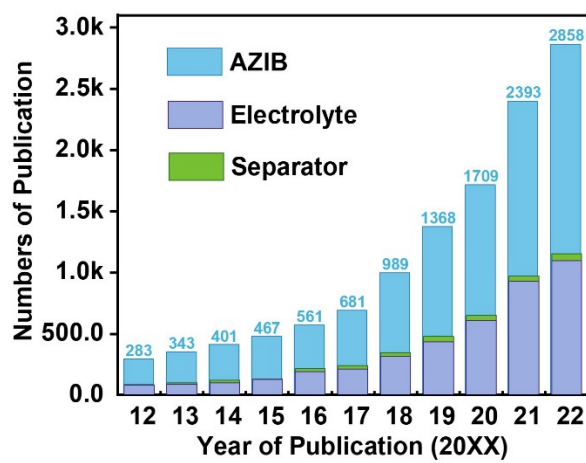


Fig. S1. Statistics of AZMBs-related papers published in the past 10 years (Data was summarized based on the Web of Science).

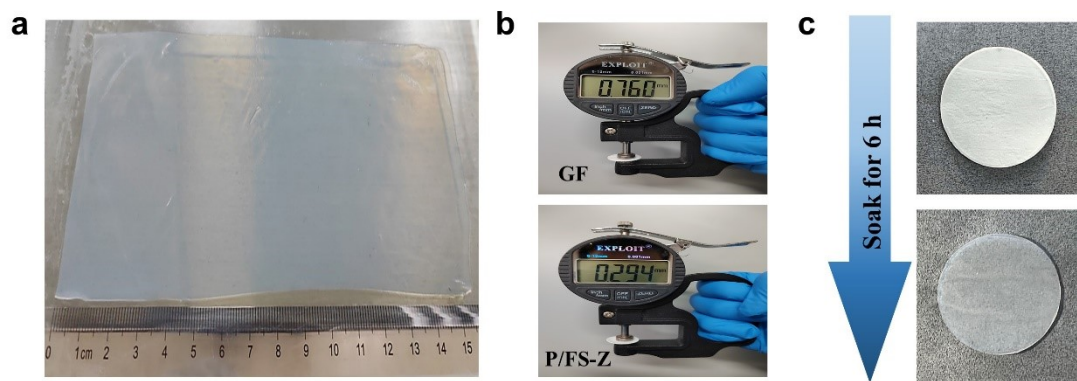


Fig. S2. Preparation method and basic properties of P/FS-Z separator. (a) Optical image. (b) Thickness difference between P/FS-Z and commercial GF separators. (c) Optical images of infiltrating of P/FS-Z separators with 2 M ZnSO_4 + 0.2 M MnSO_4 electrolytes.

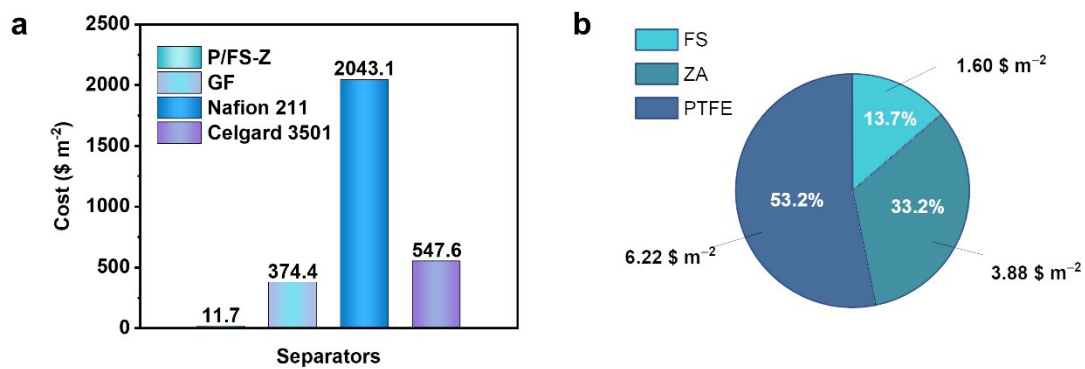


Fig. S3. (a) Cost comparison between the P/FS-Z separator and other commercial separators⁷. The statistical prices of raw materials are sourced from the suppliers in the experimental section of this work. (b) The detailed cost ratio of the raw materials for the preparation of P/FS-Z separator per m². The calculation was based on the feeding ratio of raw materials given in the experimental part and the market prices of FS (0.040 \$ g⁻¹), ZA (0.026 \$ g⁻¹), and PTFE (0.019 \$ g⁻¹) at the time of paper submission.

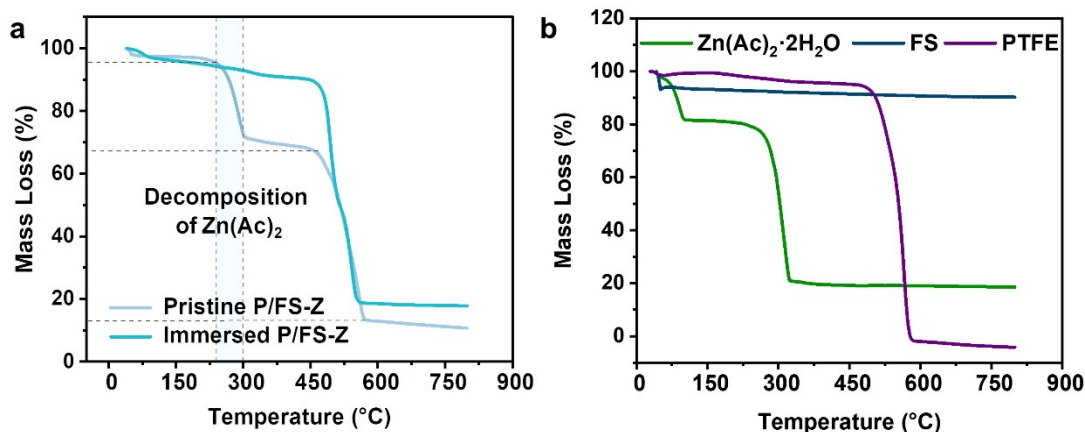


Fig. S4. TG curves of (a) P/FS-Z, (b) ZA, FS, and pure PTFE.

For the three main components in the P/FS-Z separator, zinc acetate decomposition occurred within the temperature range of 225-300 °C, and the residual product was ZnO. When the temperature was above 450 °C, PTFE begins to sublimate. The final residual product at 800 °C was ZnO+FS (residual mass is 13%). Based on the results of TG analysis, the mass fraction of FS in the P/FS-Z membrane accounts for 5.3 wt%.

As seen from the TG curves of the separators before and after soaking process shown in Fig. S4, the weight loss of $\text{Zn}(\text{Ac})_2$ decomposition process for the soaked separator is negligible, indicating that no $\text{Zn}(\text{Ac})_2$ remains in the separator after soaking process. Therefore, the $\text{Zn}(\text{Ac})_2$ salt acts as the pore former of the separator and will increase the porosity of the separator, as shown in the Table S1. If the $\text{Zn}(\text{Ac})_2$ salt was directly added into the electrolyte, the porosity of the separator without pre-added $\text{Zn}(\text{Ac})_2$ salt is lower, thereby leading to lower ionic conductivity and higher overpotential of the Zn//Zn symmetric cell.

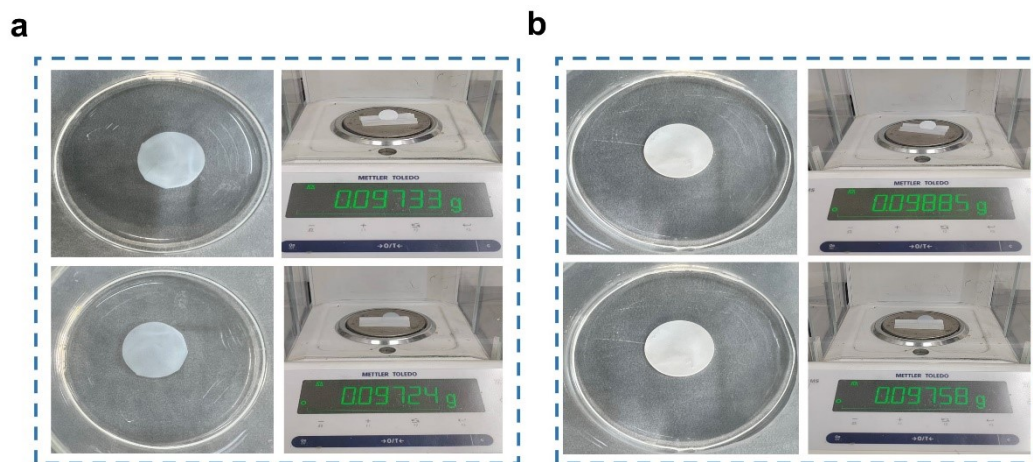


Fig. S5. Quality before (top) and after soaking for 1 days in (a) Methanol and (b) 50 wt.% H₂SO₄ solution.

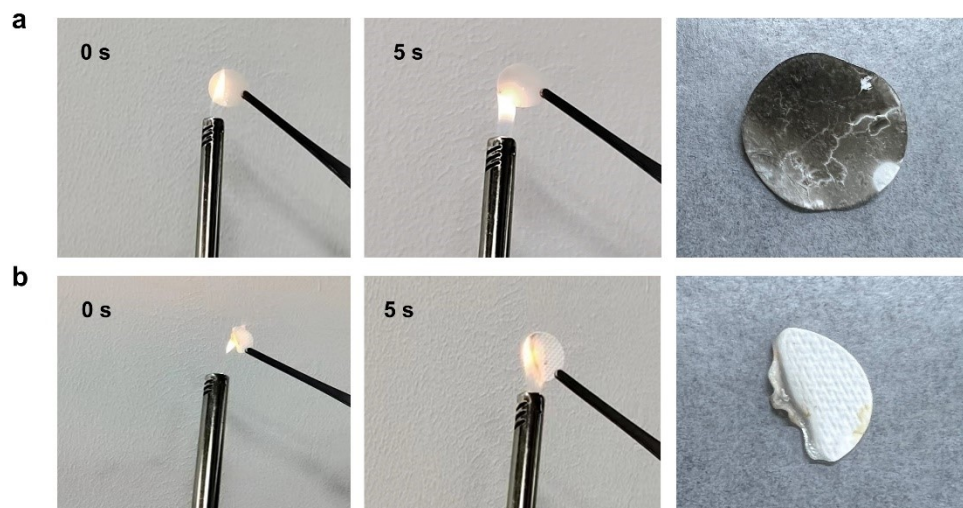


Fig. S6. Rapid ignition test of (a) P/FS-Z and (b) GF.

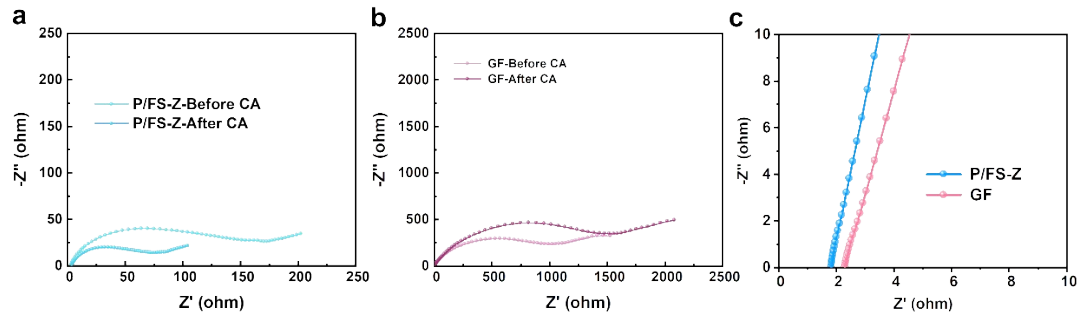


Fig. S7. EIS spectra of (a) P/FS-Z and (b) GF separators before and after the CA test.
 (c) EIS spectra of SS||SS cells with P/FS-Z and GF separator.

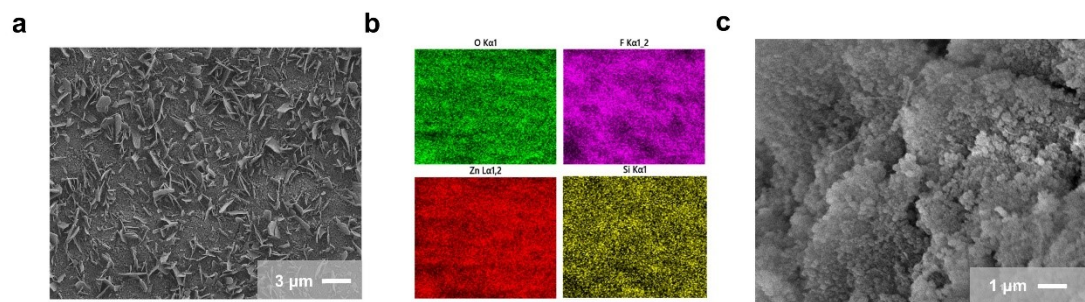


Fig. S8. SEM images of P/FS-Z separators. (a) Before soaking aqueous electrolytes, (b) EDS mapping. (c) After soaking aqueous electrolytes.

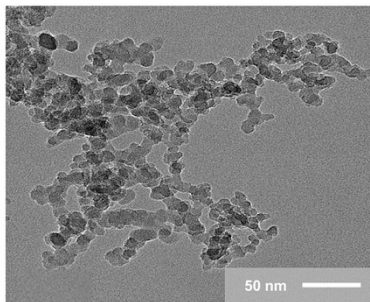


Fig. S9. TEM images of FS.

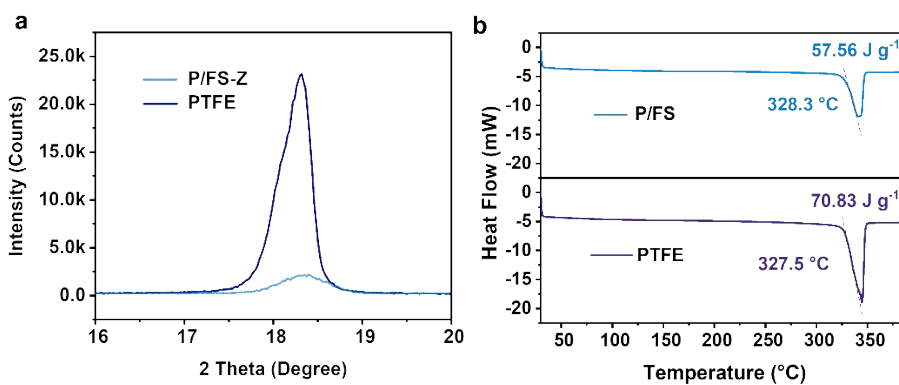


Fig. S10. (a) Enlarged diffraction peak of (100) plane of the P/FS-Z separator and

pure PTFE membrane, (b) DSC curves of the P/FS separator and pure PTFE membrane.

The composite of FS effectively reduces the crystallinity of the PTFE fibers since the obvious difference in the (100) peak intensity of PTFE corresponding to the hexagonal spiral conformation at 18.1° and the reduction of the glass transition temperature and melting enthalpy in the DSC analysis.

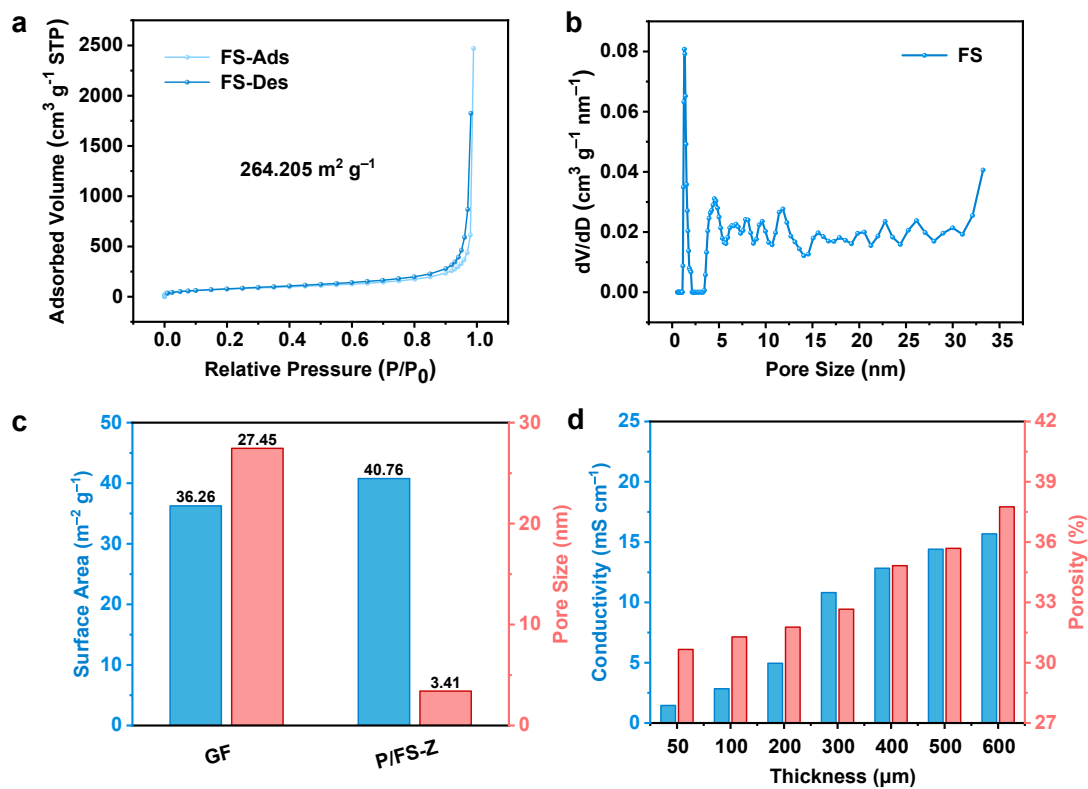


Fig. S11. Characterization of pore structure. (a) Adsorption-desorption isotherms of FS. (b) Pore size distribution of FS. (c) Specific surface area and average pore size of the GF and P/FS-Z separator. (d) Conductivity and porosity of P/FS-Z separators with different thickness.

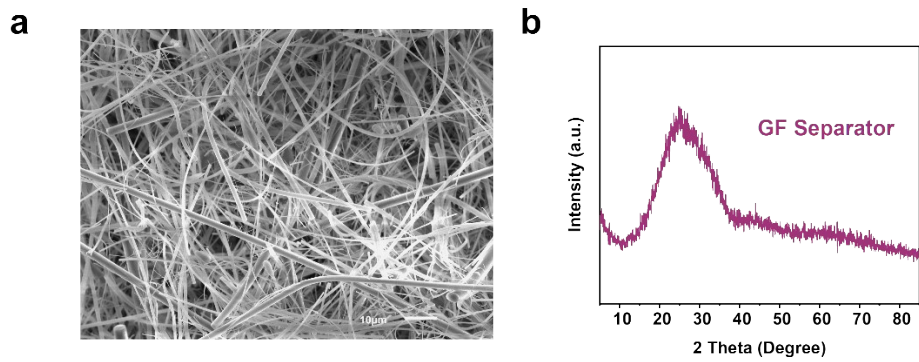


Fig. S12. (a) SEM image, and (b) XRD pattern of GF separator.

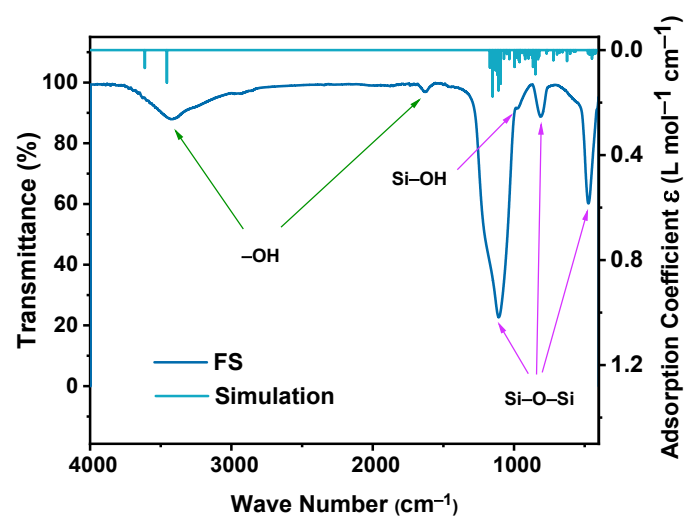


Fig. S13. ATR-FTIR spectrum and simulation curve of FS.

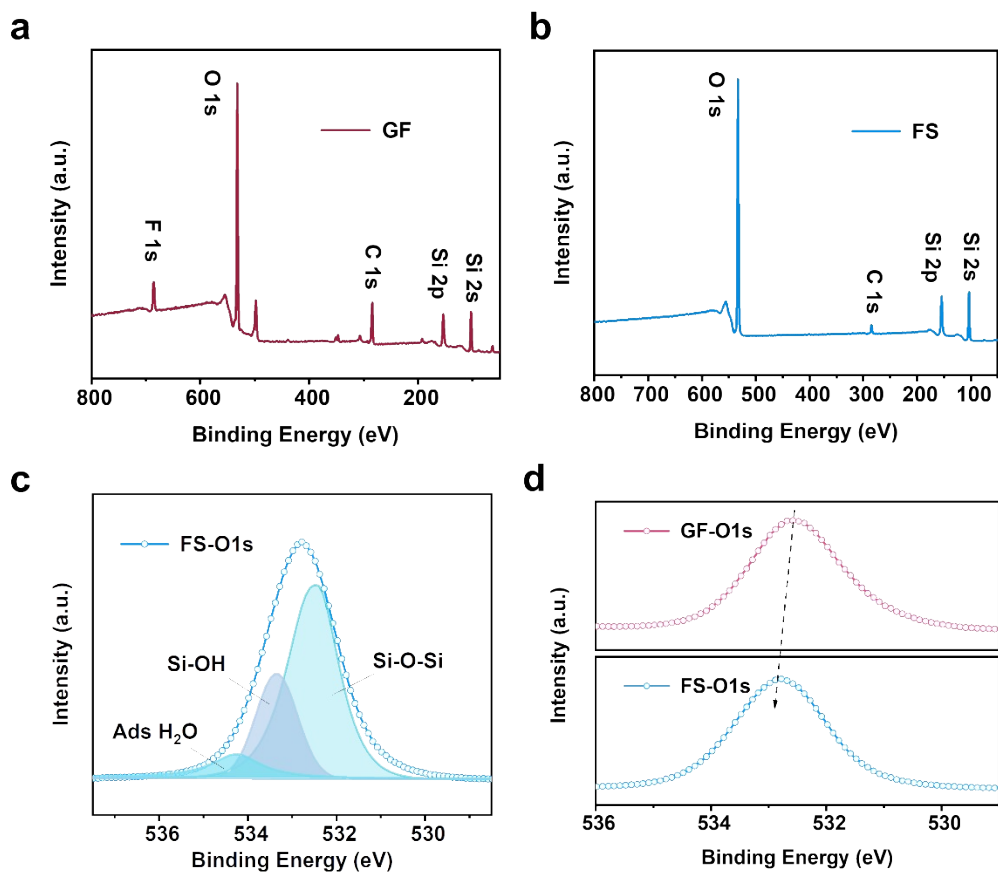


Fig. S14. XPS spectra of the P/FS-Z and GF separators. (a, b) Survey of P/FS-Z and GF separators, (c) O1s spectrum of FS, (d) Comparison of O1s spectra of the P/FS-Z and GF separators.

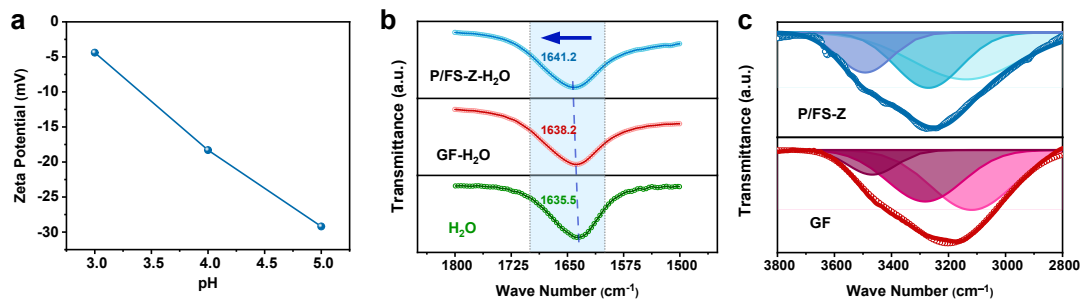


Fig. S15. The modulation effect of P/FS-Z separator on electrolytes. (a) Zeta potential of FS in different pH conditions of ZS electrolyte. ATR-FTIR spectra of (b) bending vibration mode, and (c) stretching vibration mode with GF, and P/FS-Z separators.

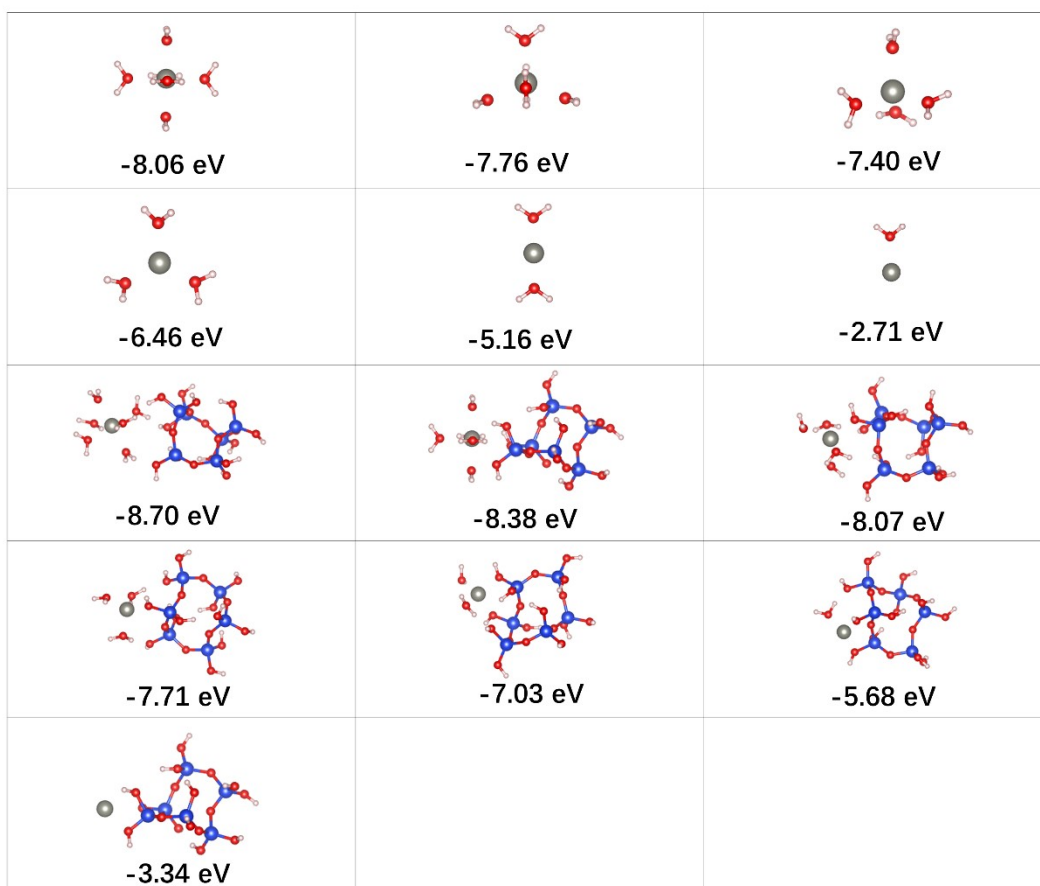


Fig. S16. Different solvation structures between Zn^{2+} and water without/with FS cluster, and corresponding solvation energy.

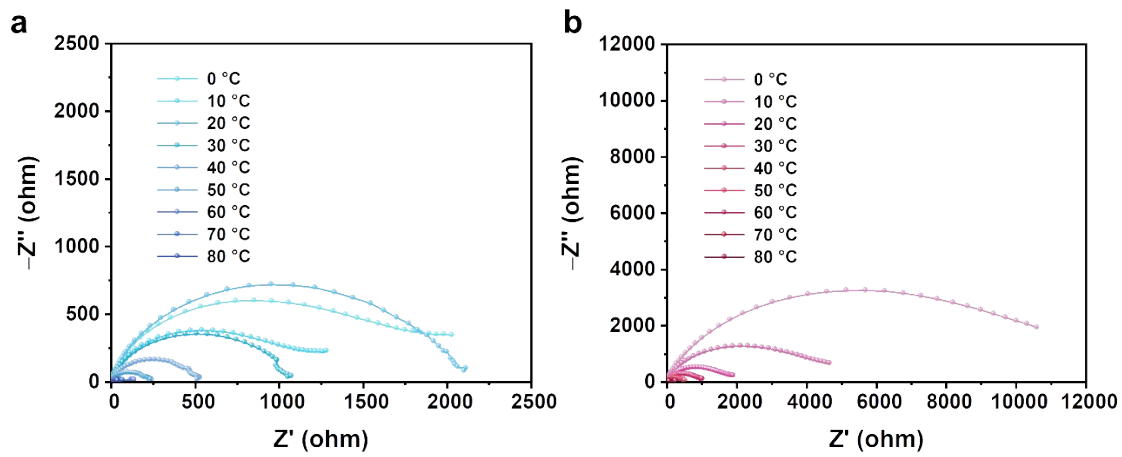


Fig. S17. EIS spectra of (a) P/FS-Z and (b) GF separators at different temperatures.

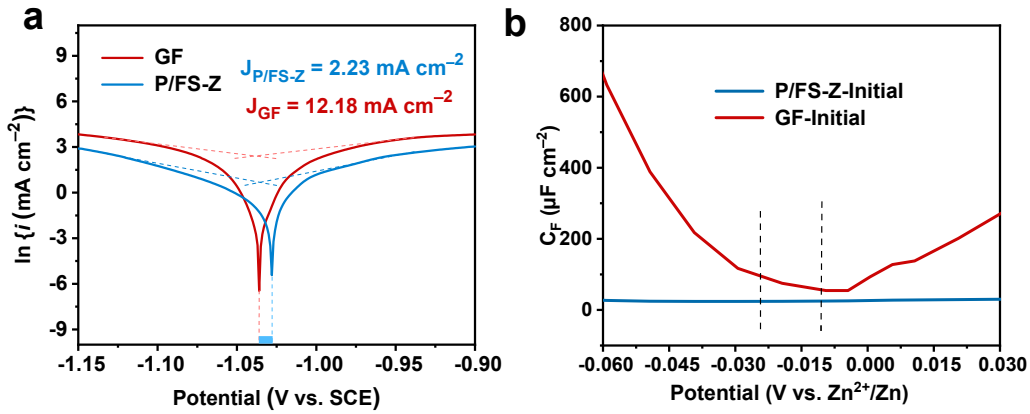


Fig. S18. Electrochemistry tests of interface between Zn anode and electrolyte modified by different separators. (a) Tafel curves, (b) Differential capacitance-potential profiles of Zn||Zn symmetric cells with GF and P/FS-Z separators.

Based on the experimental results and theoretical analysis, with the decrease of water in the $[\text{Zn}(\text{H}_2\text{O})_m]^{2+}$ solvation shell, the electrostatic attraction between the negatively charged electrode surface and the $[\text{Zn}(\text{H}_2\text{O})_m]^{2+}$ increases, leaving more Zn^{2+} in the outer Helmholtz layer (OHP). In Fig. S18b, the differential capacitance-potential curves show that the lower capacitance and negative shift in the potential of zero charge (PZC), which mean that the double layer constructed with the P/FS-Z separator is thicker, and more adsorbed Zn^{2+} on the electrode surface to effectively alleviate the concentration polarization problem under high plating capacity⁸.

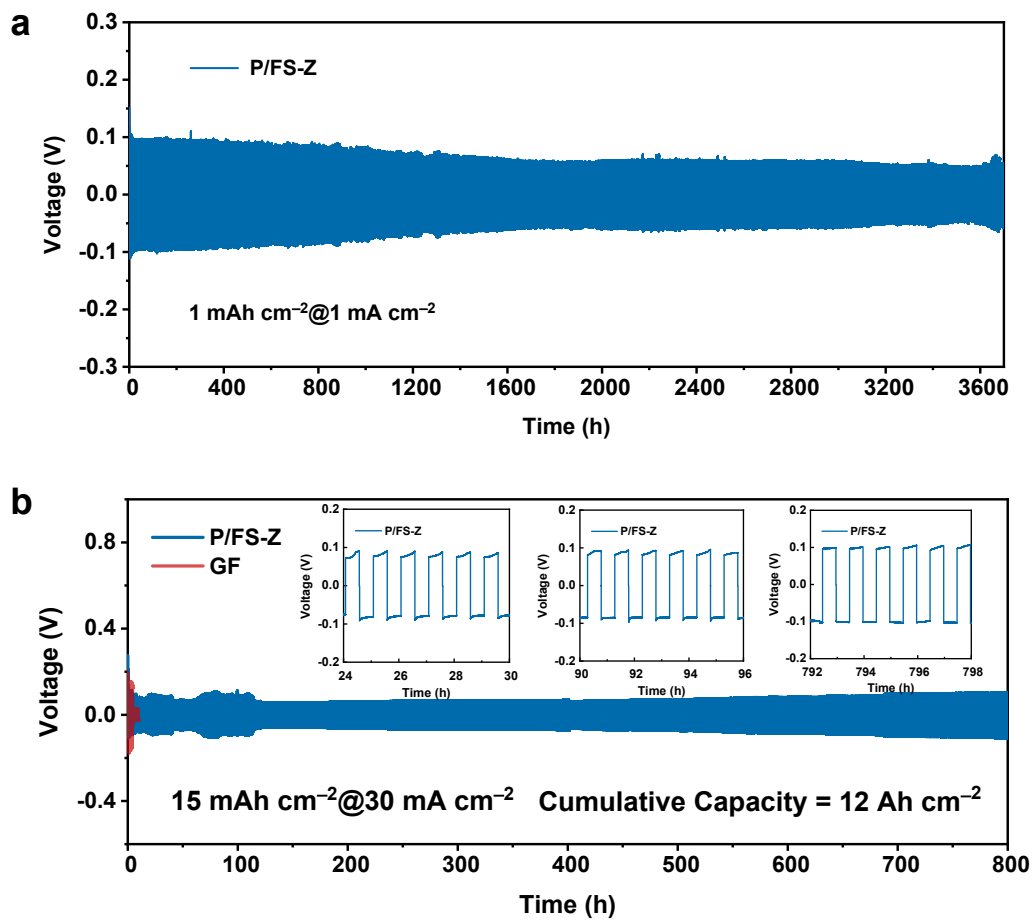


Fig. S19. Voltage-time profiles of Zn||Zn cells with P/FS-Z separator under different current densities and capacities. (a) 1 mAh cm⁻²@1 mA cm⁻². (b) 15 mAh cm⁻²@30 mA cm⁻². Insets show the enlarged view of the local polarization curve.

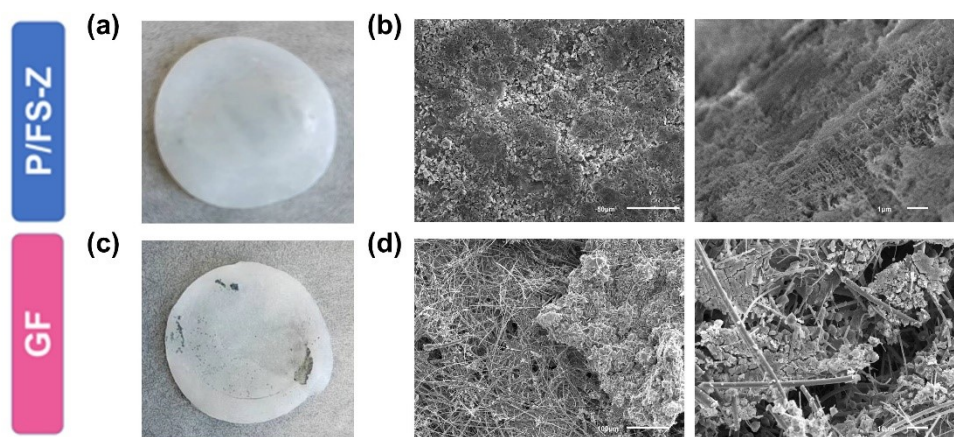


Fig. S20. Optical images and SEM images of (a, b) P/FS-Z separator, and (c, d) GF separator after 50 cycles (10 mAh cm^{-2} @ 20 mA cm^{-2}).

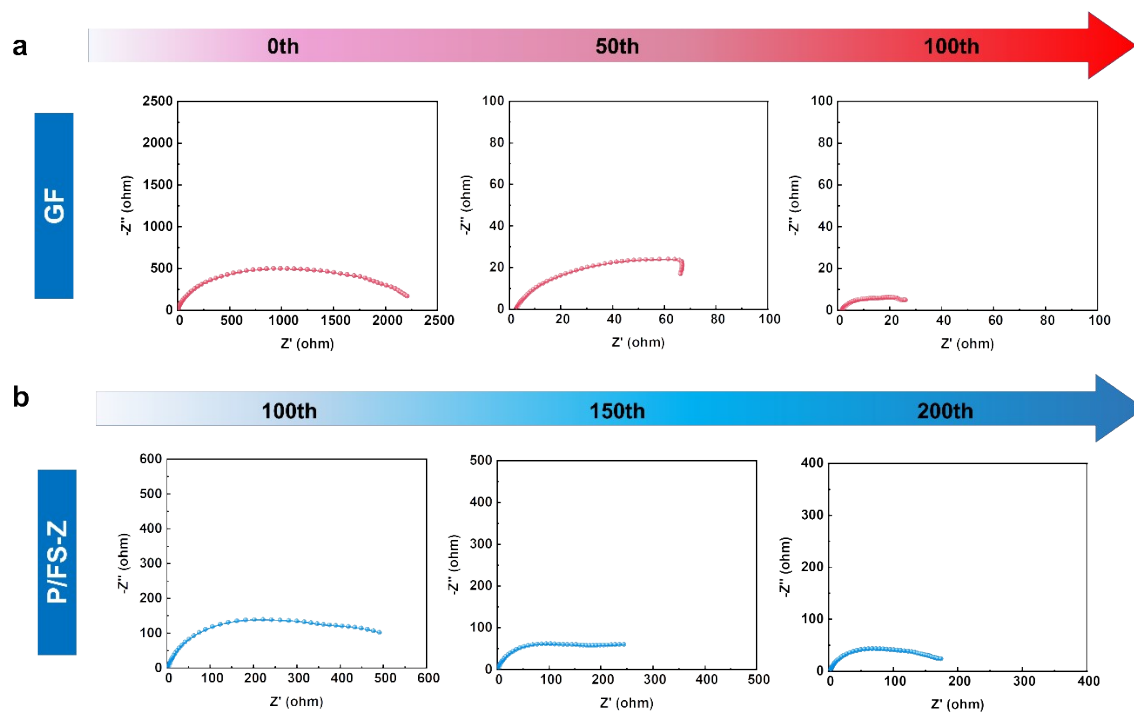


Fig. S21. EIS spectra evolution at different cycle numbers of the symmetric cell using different separators. (a) GF. (b) P/FS-Z separator.

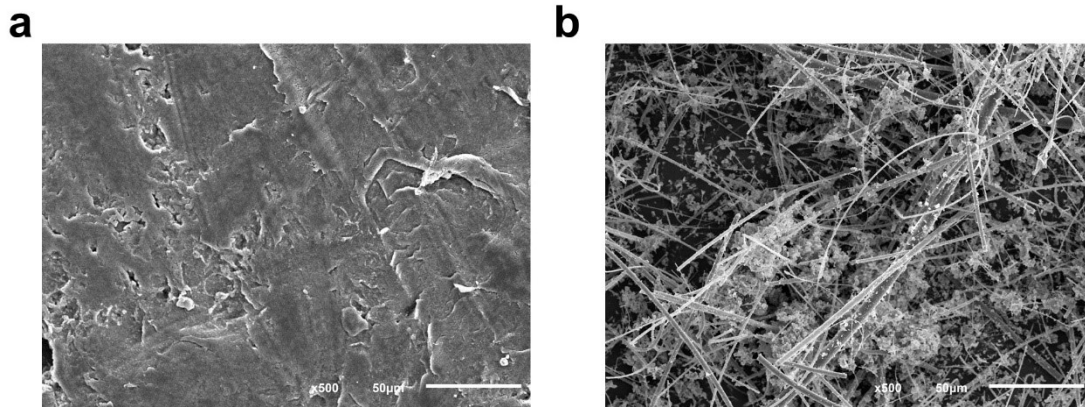


Fig. S22. SEM images of (a) P/FS-Z separator and (b) GF separator after 200 cycles (1 mAh cm^{-2} @ 5 mA cm^{-2}).

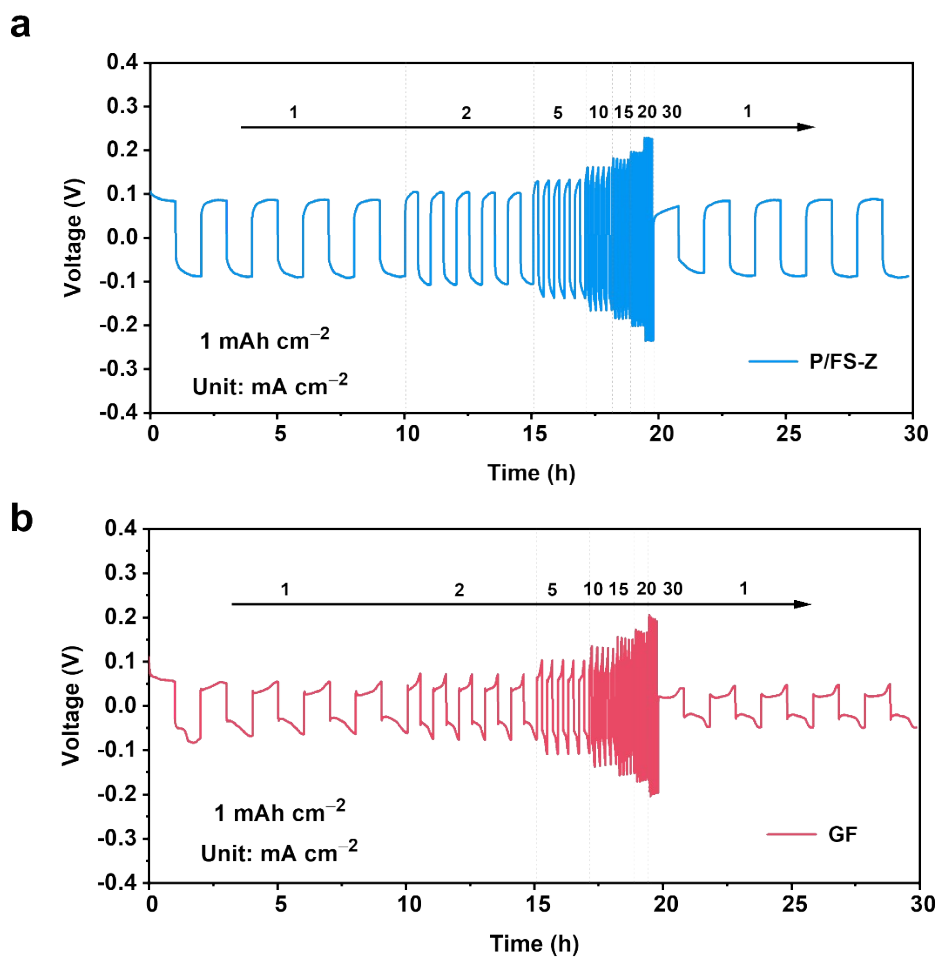


Fig. S23. Rate performance of Zn||Zn cells with (a) P/FS-Z and (b) GF separators.

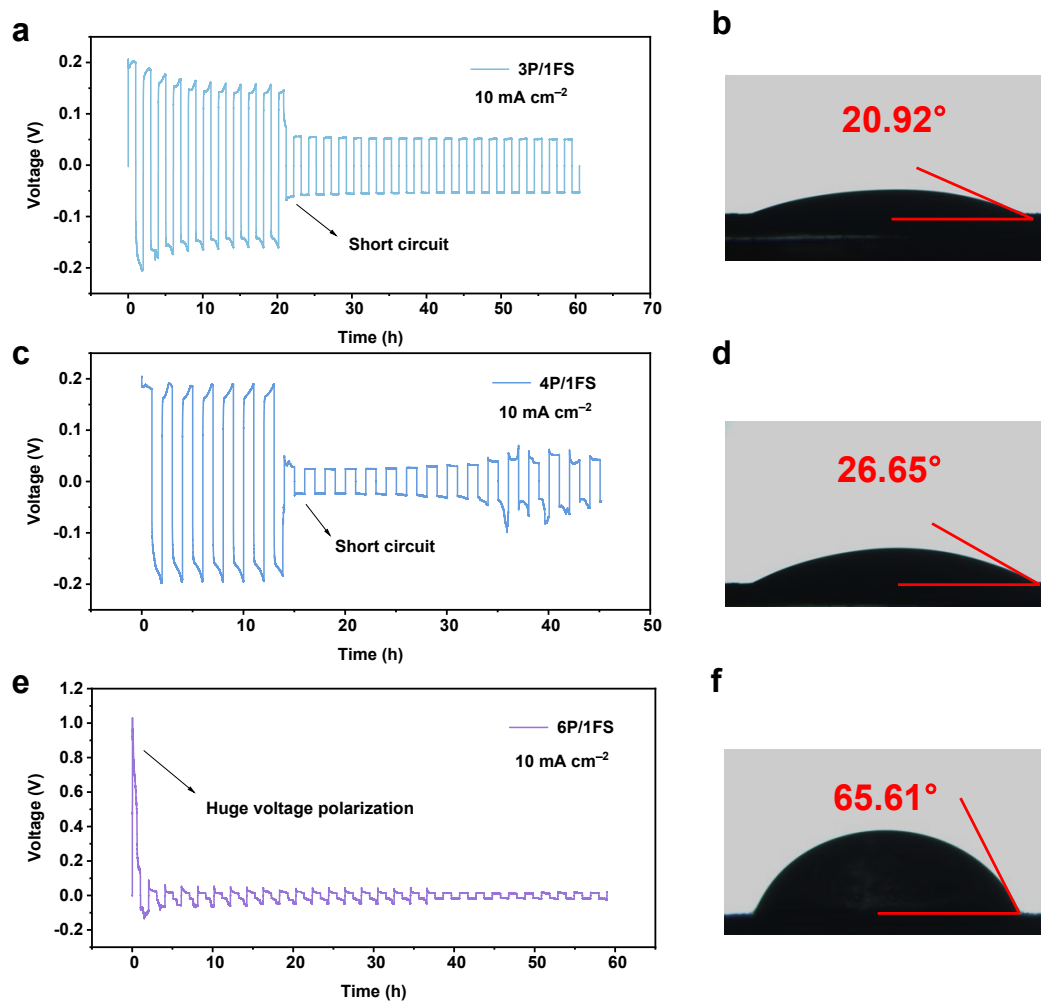


Fig. S24. Voltage-time profiles of Zn||Zn cells and contact angle tests with the P/FS-Z separators that consist of different weight ratios of PTFE and FS. (a, b) 3P/1FS. (c, d) 4P/1FS. (e, f) 6P/1FS.

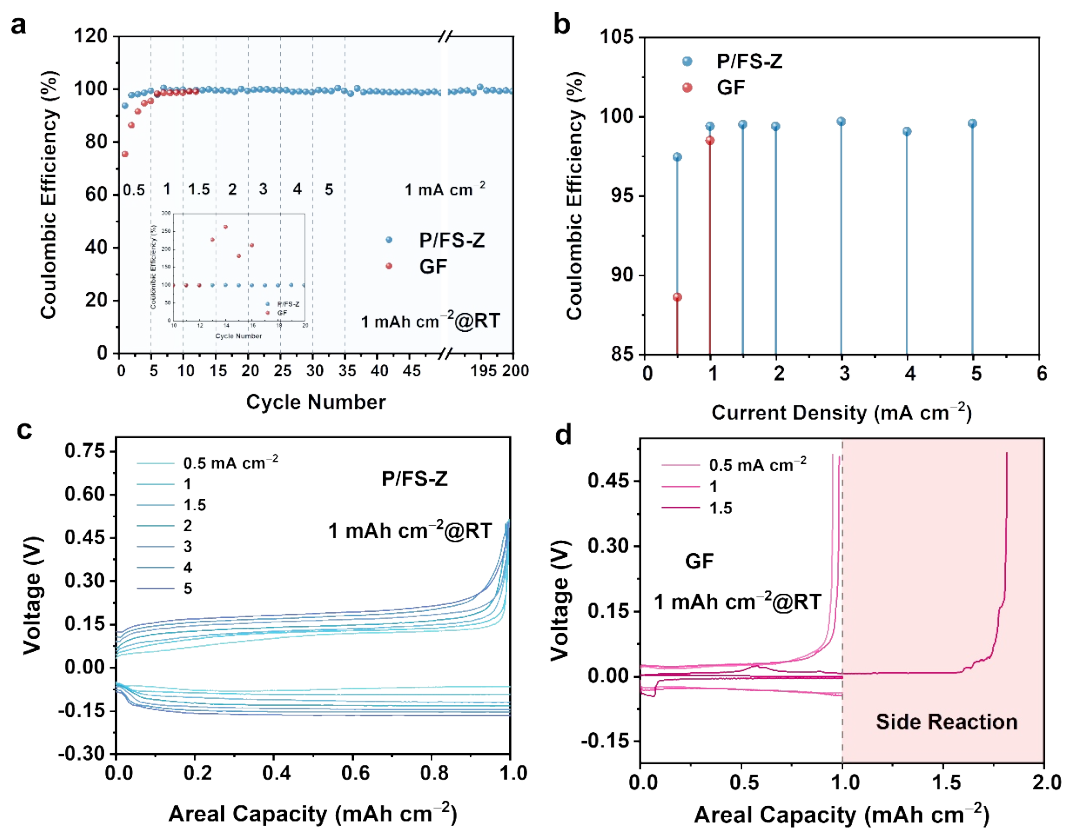


Fig. S25. Reversibility of Zn||Cu cells using different separators. (a, b) CE, and (c, d) voltage profiles of Zn||Cu using P/FS-Z and GF separators at different current densities.

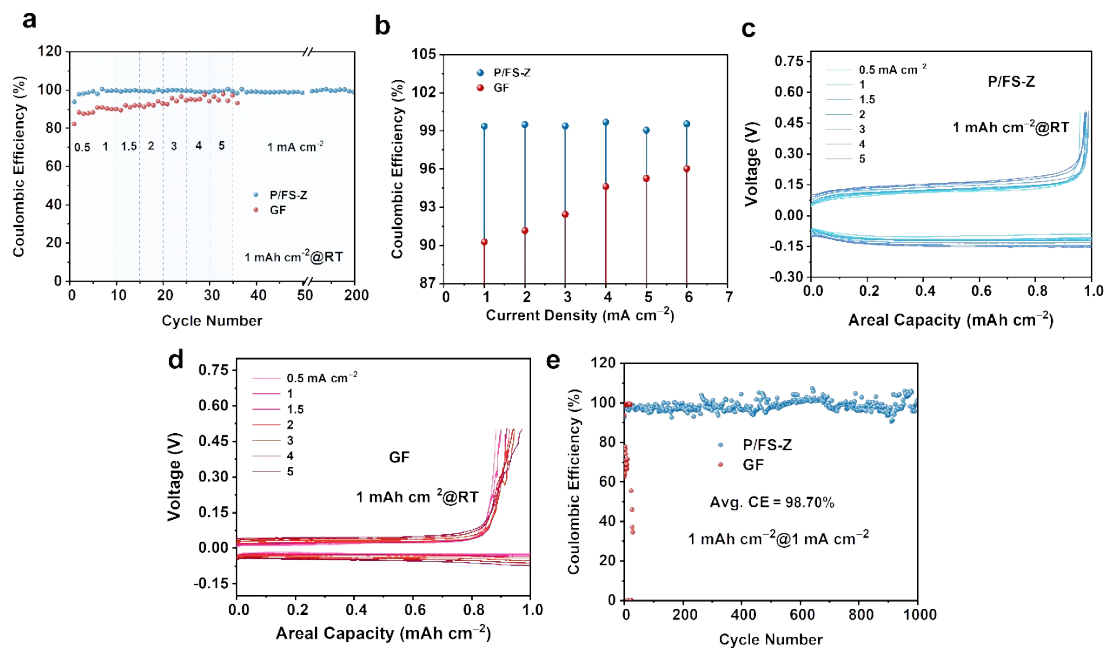


Fig. S26. Reversibility of Zn||Ti cells using different separators. (a, b) CE, and (c, d) voltage profiles of Zn||Ti using the P/FS-Z and GF separators at different current densities. e) CE versus cycle number of the Zn||Ti using different separators.

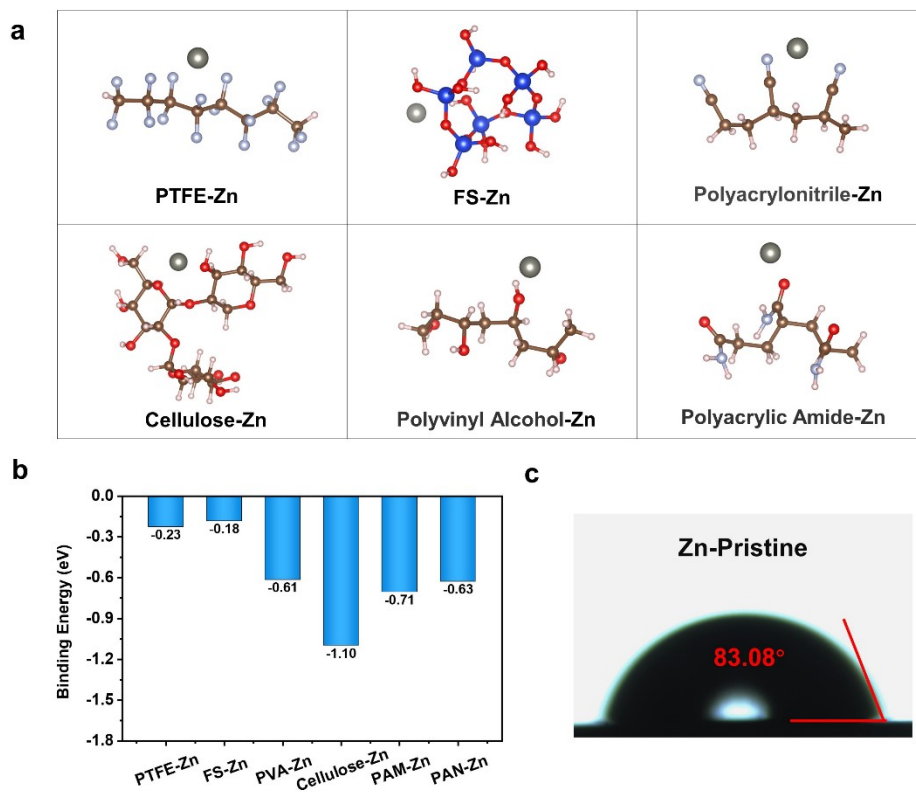


Fig. S27. The formation mechanism of the P/FS protecting layer. (a, b) Binding energy between Zn with PTFE, FS, polyacrylonitrile, cellulose, polyvinyl alcohol, and polyacrylamide. (c) Contact angle of the electrolyte on bare Zn.

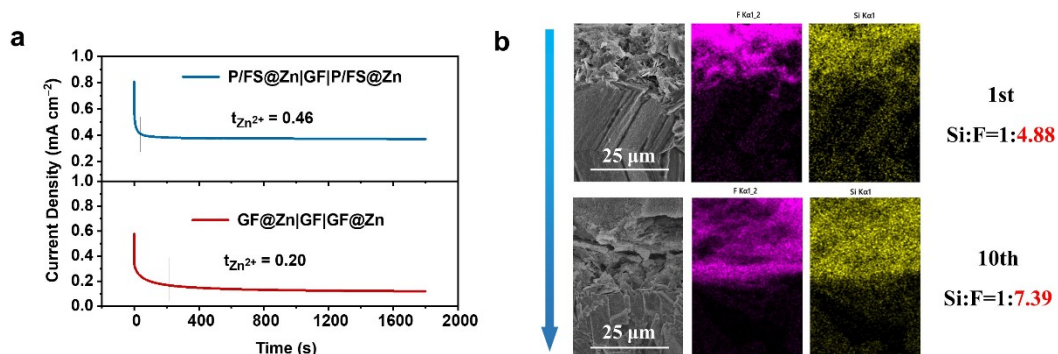


Fig. S28. The phenomenon of P/FS protecting layer formed on the surface of cycled Zn anodes. (a) CA tests with Zn anodes cycled for 1 cycle ($5 \text{ mAh cm}^{-2}@10 \text{ mA cm}^{-2}$) using brand-new GF separators. (b) The EDS mapping of the cross-section of Zn anodes surface after 1 cycle and 10 cycles ($5 \text{ mAh cm}^{-2}@10 \text{ mA cm}^{-2}$).

The Zn||Zn symmetric cells with P/FS-Z and GF separators that were pre-cycled for 1 cycle were disassembled and the Zn electrodes were vacuum-dried and labeled as P/FS@Zn and GF@Zn. After that, the P/FS@Zn||P/FS@Zn and GF@Zn||GF@Zn symmetric cell were reassembled with same new GF separators for CA testing. As seen from Fig. S28a, the P/FS@Zn||P/FS@Zn shows higher transference number of Zn^{2+} , which indirectly indicates that some functional layer was formed on the Zn electrode when matched with the P/FS-Z separator.

Further, the surface layer on the Zn electrode was quantified by the SEM equipped with the EDS mapping. As shown in Fig. S28b, it is clear that the surface of Zn electrode was covered with Si- and F-containing species. Moreover, the content of F dominates and increases with cycling, indicating that the surface layer indeed forms and is hydrophobic.

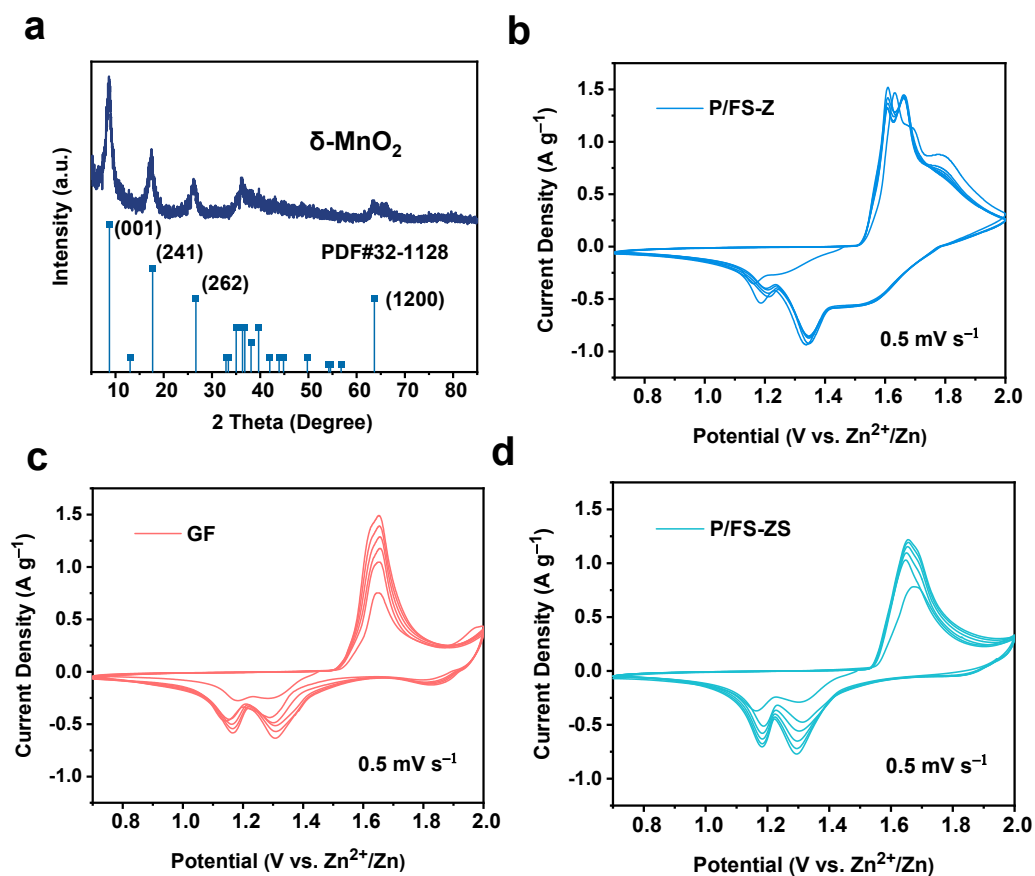
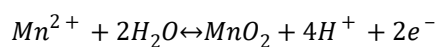


Fig. S29. Electrode materials and corresponding CV behaviors using different separators. (a) The XRD patterns of δ -MnO₂ cathode. (b-d) CV curves of the Zn|| δ -MnO₂ full cells using different separators.

According to previous literature reports⁹⁻¹², the reversible high voltage wide peaks can be attributed to the valence change reaction of Mn²⁺/Mn⁴⁺ under the complexation of acetate anion:



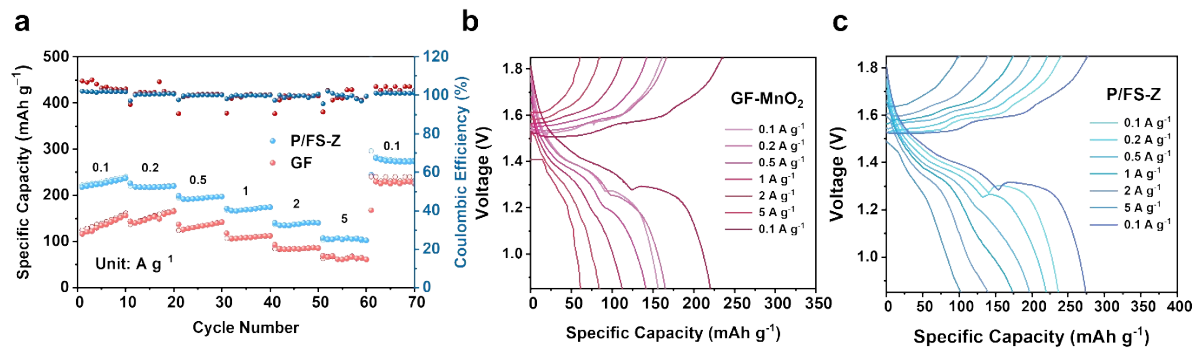


Fig. S30. (a) Rate performances. (b, c) GCD profiles at different rates.

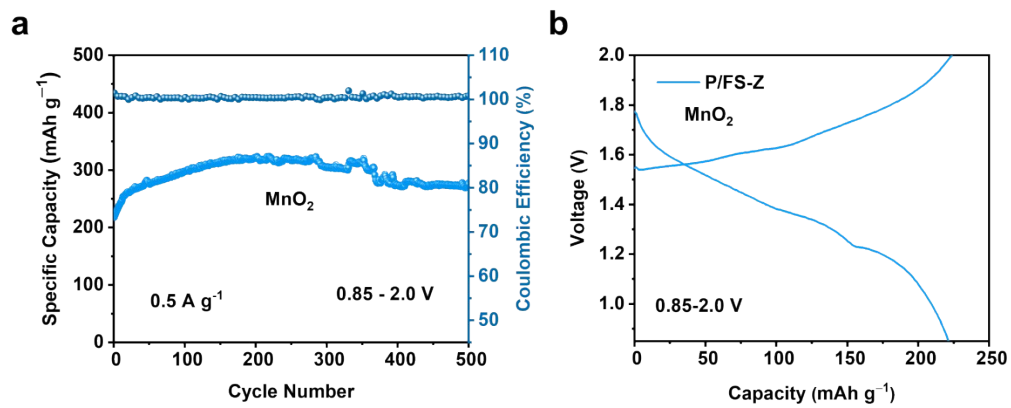


Fig. S31. (a) Cycling performance, and (b) GCD curves of Zn||MnO₂ full cell cycling within a voltage window of 0.85-2 V.

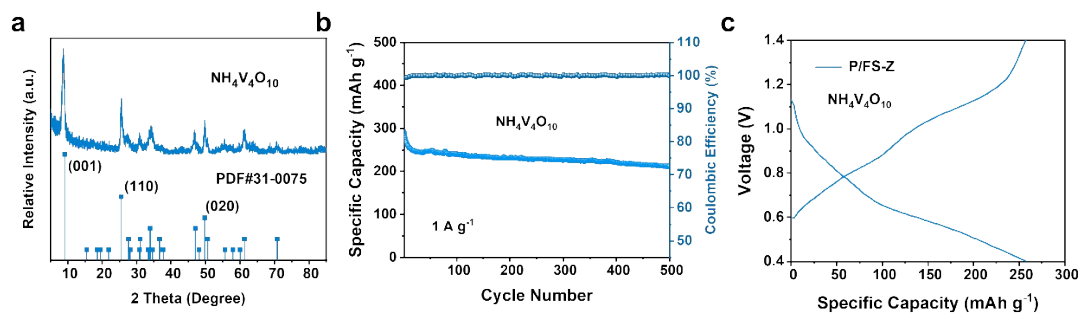


Fig. S32. (a) XRD patterns, (b) Cycling performance, and (c) GCD profiles of $\text{NH}_4\text{V}_4\text{O}_{10}$.

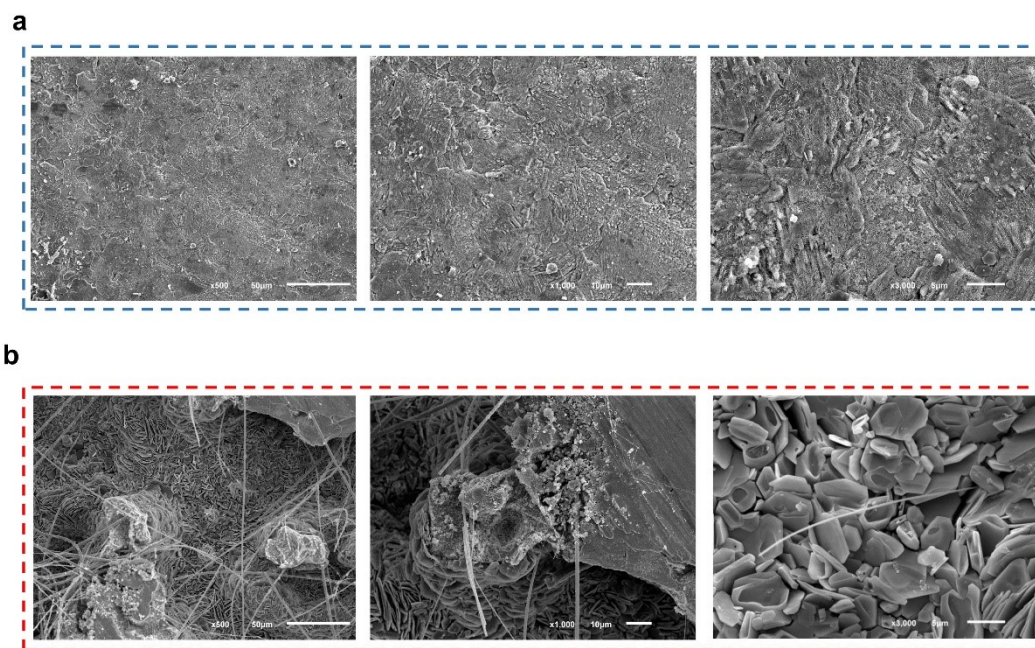


Fig. S33. SEM images of the cycled Zn anodes in Zn||MnO₂ full cells with (a) P/FS-Z and (b) GF separators.

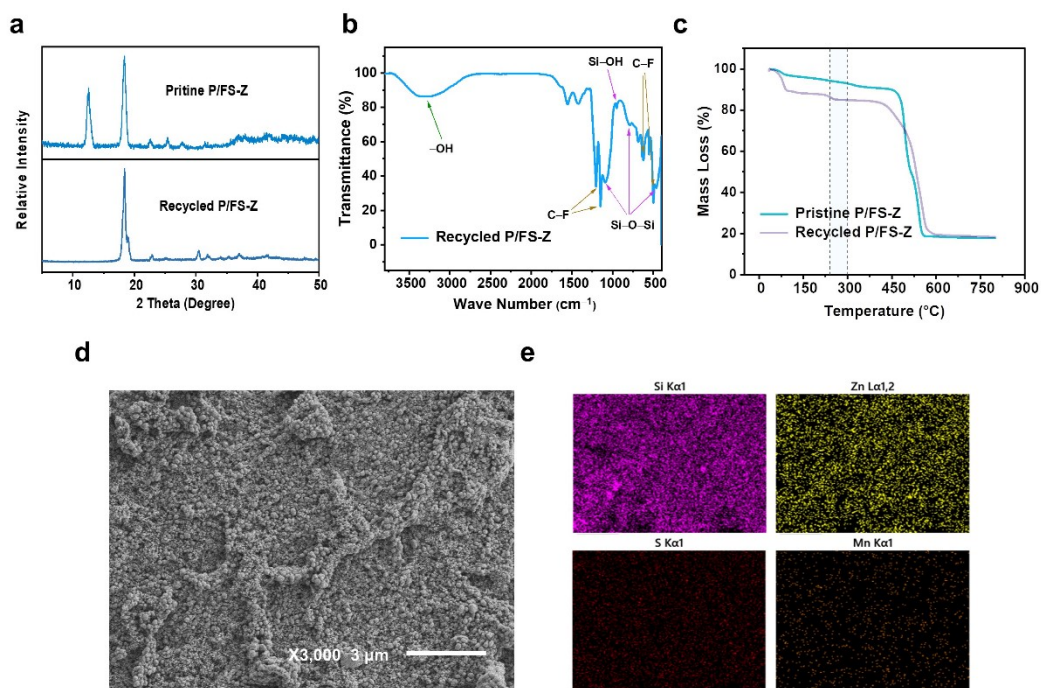


Fig. S34. (a) XRD, (b) ATR-FT-IR spectrum, (c) TG, (d) SEM, and (e) Element distribution of Si, S, Mn, Zn of recycled P/FS-Z separator.

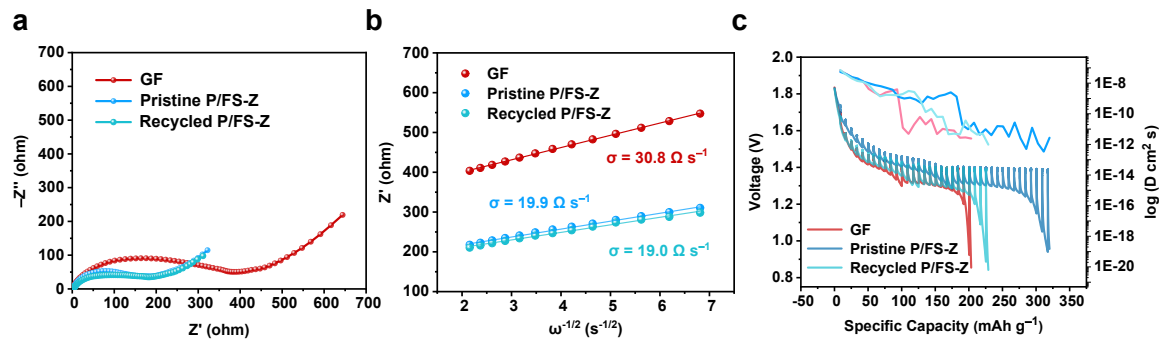


Fig. S35. (a) EIS spectra, (b) Warburg coefficient fitting, and (c) GITT test of Zn||MnO₂ with GF, pristine P/FS-Z, and recycled P/FS-Z separators.

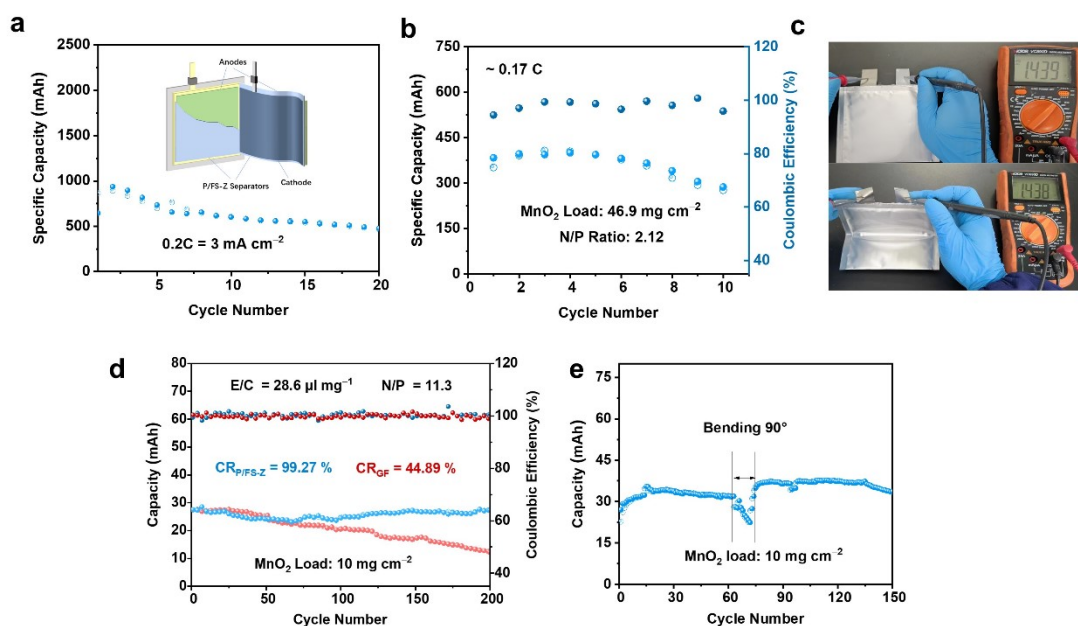


Fig. S36. Zn||MnO₂ pouch cells with P/FS-Z separators under different extreme working conditions. (a) Cycling performance of high-energy density pouch cell and its structure (Inset). (b) Cycling performance of pouch cell with mass loading (MnO₂ load: 46.9 mg cm⁻²) (c) Open circuit voltage under 90° for pouch cell. (d) Cycling performance of wearable pouch cell. (e) Cycling performance under 0° and 90° bending condition of wearable pouch cell.

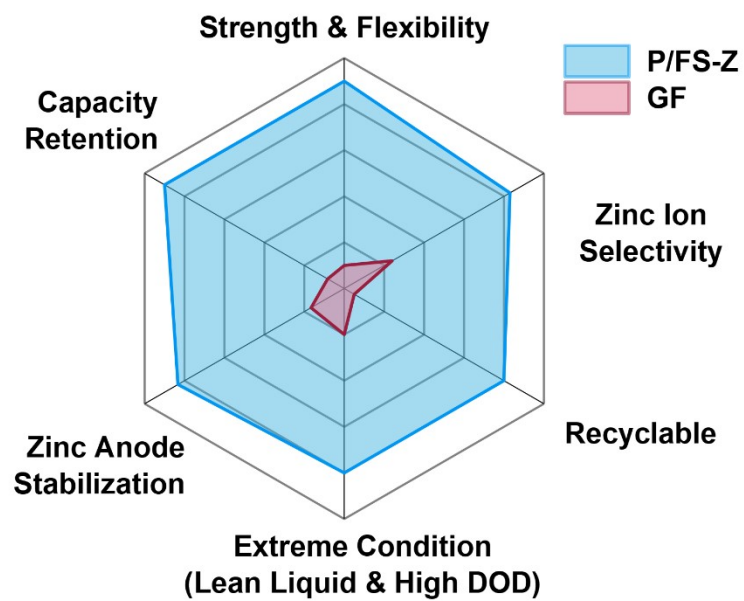


Fig. S37. Comprehensive comparison of the battery performance of P/FS-Z and GF separators.

Tables

Table. S1. The porosity and ionic conductivity of the separators with and without Zn(Ac)₂ salt and the overpotential of the symmetric cells using the different separators.

Separator	Porosity (%)	Ionic conductivity (mS cm ⁻¹)	Overpotential (mV)
P/FS	22.46	3.49	133 mV
P/FS-Z	32.66	10.82	101 mV

Table. S2. Comparison of the conductivity, R_{ct}, overpotential (1 mAh cm⁻²@1 mA cm⁻²), and costs of the separators as-prepared using different oxides as the fillers.

Fillers	Conductivity (mS cm ⁻¹)	R _{ct} of Zn Zn cells (Ω)	Overpotential (mV)	Cost (\$ kg ⁻¹)
ZnO	7.93	840.7	113	126.3
MgO	6.12	235.2	167	216.3
ZrO ₂	0.81	169.3	105	128.8
TiO ₂	4.57	508.3	149	59.1
SnO ₂	3.36	711.0	134	140.7
MoO ₃	2.95	288.2	75	57.5
Al ₂ O ₃	6.26	762.5	124	96.9
Bi ₂ O ₃	2.71	1539.0	153	140.5
Sb ₂ O ₅	4.64	125.0	68	97.1
Nb ₂ O ₅	2.18	126.7	116	155.7
FS	10.75	249.0	101	40.6

Table. S3. Element distribution of O, F, Si, and Zn of pristine P/FS-Z separator.

Element	Line Series	Apparent Concentration	K Ratio	wt%	Atom%
O	K	25.16	0.08468	17.70	29.04
F	K	71.23	0.13986	36.39	50.29
Si	K	2.61	0.02066	4.17	3.90
Zn	L	17.51	0.17507	41.73	16.76
Total	/	/		100.00	100.0

Table. S4. Element distribution of O, F, Si, S, Mn, and Zn of recycled P/FS-Z separator.

Element	Line Series	Apparent Concentration	K Ratio	wt%	Atom%
O	K	14.53	0.04890	12.83	15.26
F	K	118.98	0.23362	79.75	79.89
Si	K	2.94	0.02332	6.68	4.53
S	K	0.17	0.00149	0.38	0.22
Mn	K	0.00	0.00000	0.00	0.00
Zn	L	0.06	0.00058	0.36	0.11
Total	/			100.00	100.00

Table. S5. Comparison of cumulative capacities for Zn||Zn symmetrical cells between this work and previous reports using various separators strategies.

Strategy	Current density (mA cm ⁻²)	Areal capacity (mAh cm ⁻²)	Lifespan (h)	Accumulative areal capacity (mAh cm ⁻²)	References
CP-GF	5	5	500	1250	13
Cellulose/GO	20	10	400	4000	14
NC/GF	10	10	360	1800	15
WP-GF	9	4.5	850	3825	16
ZSM-5/GF	1	1	2000	1000	17
VG-Janus separator	10	1	600	3000	18
ZC	5	2.5	1000	2500	19
CS-filter paper	5	1	450	1125	20
PTC/GF	10	5	550	2750	21
CT separator	20	2	150	1500	22
Mxene@NiO	10	10	500	2500	23
DIE separator	10	2.5	1600	8000	24
Zn-BTC separator	5	2.5	350	875	25
SiO ₂ coated GF	5	1	1000	2500	26
UCNF	10	2	600	3000	27
LCNF	8	8	300	1200	28
SP	20	10	100	1000	29
Uio-66-GF	2	1	1650	1650	30
IS/SiO ₂ -OH@GF	10	1	2600	13000	31
PG	15	5	4200	31500	32
Janus separator	10	10	1400	7000	33
PNGF	10	4	400	2000	34
P/FS-Z	20	10	1200	12000	This work
P/FS-Z	30	15	800	12000	This work

Table. S6. Comparison of the basic properties of the separators in the previous reports and this work.

Strategy	Thickness (μm)	Electrolytes	Electrolyte Uptake (%)	Porosity (%)	Weight of Separator and Electrolyte (mg)	References
CP-GF	290	2 M ZnSO ₄	34.2	\	~140	13
Cellulose/GO	30	2 M Zn(CF ₃ SO ₃) ₂	575	517	~230	14
WP-FP	327	3 M Zn(CF ₃ SO ₃) ₂	\	\	\	16
VG-Janus separator	200	2 M ZnSO ₄	\	\	\	18
ZC	50	2 M ZnSO ₄	379	\	~190	19
PTC/GF	~300	2 M ZnSO ₄	\	\		21
CT	415	2 M ZnSO ₄ + 0.1 M MnSO ₄	\	248%		22
UCNF	20	2 M ZnSO ₄	195	90%	~150	27
LCNF	59.3	3 M Zn(CF ₃ SO ₃) ₂	521.1	\	~240	28
SP	80	2 M Zn(CF ₃ SO ₃) ₂	813	91.4	~280	29
VVLP	\	2M ZnSO ₄	\	\	\	35
PG	69	2 M Zn(CF ₃ SO ₃) ₂	2267	\	~260	32
Janus separator	260	3 M ZnSO ₄	\	\	\	33
PNGF	263	2 M ZnSO ₄	\	\	\	36
P/FS-Z	294	2 M ZnSO ₄	31.5	33.2	121	This work

Table. S7. Comparison of high-DOD Zn||Zn symmetric cell cycling performance between this work and the previous reports using various separators strategies.

Strategy	DOD (%)	Cycle Numbers	References
ZnHAP/BC	50	7	7
CNF-SO ₃ Zn	80	7	37
WP-GF	78	33	16
P/FS-Z	80	75	This work

Table. S8. Comparison of cycling performance for pouch-cells between this work and previous reports using various separators strategies.

Strategy	Cathodes	Mass Loading (mg cm ⁻²)	Cycle Numbers	Capacity Retention (%)	References
CP-GF	NH ₄ V ₄ O ₁₀	/	450	85% (after activation)	13
Cellulose/GO	MnO ₂	/	200	73%	14
ZC	MnO ₂	/	50	~70%	19
PG	Zn _{0.27} V ₂ O ₅	/	50	85.2%	32
CNF-SO ₃ Zn	PANI	17	150	95%	37
Janus separator	NH ₄ V ₄ O ₁₀	/	270	87.4%	33
P/FS-Z	MnO ₂	14.3	200	99.27%	This work

Table. S9. Cell parameters for the pouch cell with high mass loading.

Physical parameter	Values	Electrochemical parameter	Values
Zn anode (20 μm)	0.92 g	Specific capacity	173.51 mAh g ⁻¹
Cu collector	1.42 g	Cell average voltage	1.30 V
Cathode	9.02 g	Capacity	936.9 mAh
P/FS-Z Separator	8.97 g	Energy	1.214 Wh
P/FS-Z Separator + Electrolyte	21.66 g	Active area	64 cm ²
Others' weight	2.17 g	E/C ratio	2.34 $\mu\text{l mg}^{-1}$
Pouch-cell weight	35.19 g	Energy density	34.50 Wh kg ⁻¹

References:

1. C. Li, X. Chi, J. Huang, J. Wu and Y. Liu, *Acs Applied Energy Materials*, 2022, DOI: 10.1021/acsaem.1c02853.
2. Y. Marcus, *Chemical Reviews*, 2009, **109**, 1346-1370.
3. F. Neese, *WIREs Computational Molecular Science*, 2022, **12**, e1606.
4. S. Grimme, S. Ehrlich and L. Goerigk, *Journal of Computational Chemistry*, 2011, **32**, 1456-1465.
5. A. V. Marenich, C. J. Cramer and D. G. Truhlar, *The Journal of Physical Chemistry B*, 2009, **113**, 6378-6396.
6. T. Lu and F. Chen, *J Comput Chem*, 2012, **33**, 580-592.
7. H. Qin, W. Chen, W. Kuang, N. Hu, X. Zhang, H. Weng, H. Tang, D. Huang, J. Xu and H. He, *Small*, 2023, DOI: 10.1002/sml.202300130, e2300130.
8. H. Yang, D. Chen, R. Zhao, G. Li, H. Xu, L. Li, X. Liu, G. Li, D. Chao and W. Han, *Energy & Environmental Science*, 2023, DOI: 10.1039/D3EE00658A.
9. X. Zeng, J. Liu, J. Mao, J. Hao, Z. Wang, S. Zhou, C. D. Ling and Z. Guo, *Advanced Energy Materials*, 2020, **10**, 1904163.
10. Z. Liu, L. Li, L. Qin, S. Guo, G. Fang, Z. Luo and S. Liang, *Advanced Materials*, 2022, **34**, 2204681.
11. Z. Liu, Y. Yang, S. Liang, B. Lu and J. Zhou, *Small Structures*, 2021, **2**, 2100119.
12. Z. Zhong, J. Li, L. Li, X. Xi, Z. Luo, G. Fang, S. Liang and X. Wang, *Energy Storage Materials*, 2022, **46**, 165-174.
13. Z. Yang, W. Li, Q. Zhang, C. Xie, H. Ji, Y. Tang, Y. Li and H. Wang, *Materials Today Energy*, 2022, **28**, 101076.
14. J. Cao, D. Zhang, C. Gu, X. Wang, S. Wang, X. Zhang, J. Qin and Z.-S. Wu, *Advanced Energy Materials*, 2021, **11**, 2101299.
15. X. Yang, W. Li, J. Lv, G. Sun, Z. Shi, Y. Su, X. Lian, Y. Shao, A. Zhi, X. Tian, X. Bai, Z. Liu and J. Sun, *Nano Research*, 2021, DOI: 10.1007/s12274-021-3957-z.
16. Y. Guo, W. Cai, Y. Lin, Y. Zhang, S. Luo, K. Huang, H. Wu and Y. Zhang, *Energy Storage Materials*, 2022, **50**, 580-588.
17. J. Zhu, Z. Bie, X. Cai, Z. Jiao, Z. Wang, J. Tao, W. Song and H. J. Fan, *Advanced Materials*, 2022, **34**, 2207209.
18. C. Li, Z. Sun, T. Yang, L. Yu, N. Wei, Z. Tian, J. Cai, J. Lv, Y. Shao, M. H. Rummeli, J. Sun and Z. Liu, *Advanced Materials*, 2020, **32**, 2003425.
19. J. Cao, D. Zhang, C. Gu, X. Zhang, M. Okhawilai, S. Wang, J. Han, J. Qin and Y. Huang, *Nano Energy*, 2021, **89**, 106322.
20. X. Yang, W. Wu, Y. Liu, Z. Lin and X. Sun, *Chemical Engineering Journal*, 2022, **450**, 137902.
21. Y. Zhang, T. Zhao, S. Yang, Y. Zhang, Y. Ma and Z. Wang, *Journal of Energy Chemistry*, 2022, **75**, 310-320.
22. P. Cao, H. Zhou, X. Zhou, Q. Du, J. Tang and J. Yang, *ACS Sustainable Chemistry & Engineering*, 2022, **10**, 8350-8359.

23. Y. An, Y. Tian, Q. Man, H. Shen, C. Liu, Y. Qian, S. Xiong, J. Feng and Y. Qian, *ACS Nano*, 2022, **16**, 6755-6770.
24. Y. Liang, D. Ma, N. Zhao, Y. Wang, M. Yang, J. Ruan, G. Yang, H. Mi, C. He and P. Zhang, *Advanced Functional Materials*, 2022, **32**, 2112936.
25. H. Yang, Y. Qiao, Z. Chang, H. Deng, P. He and H. Zhou, *Advanced Materials*, 2020, **32**, 2004240.
26. Y. Yang, T. Chen, M. Zhu, G. Gao, Y. Wang, Q. Nie, Y. Jiang, T. Xiong, W. S. V. Lee and J. Xue, *ACS Applied Materials & Interfaces*, 2022, **14**, 37759-37770.
27. Y. Li, X. Peng, X. Li, H. Duan, S. Xie, L. Dong and F. Kang, *Adv Mater*, 2023, DOI: 10.1002/adma.202300019, e2300019.
28. Z. Li, L. Ye, G. Zhou, W. Xu, K. Zhao, X. Zhang, S. Hong, T. Ma, M.-C. Li, C. Liu and C. Mei, *Chemical Engineering Journal*, 2023, **457**.
29. W. Hu, J. Ju, Y. Zhang, W. Tan, N. Deng, W. Liu, W. Kang and B. Cheng, *Journal of Materials Chemistry A*, 2022, **10**, 24761-24771.
30. Y. Song, P. Ruan, C. Mao, Y. Chang, L. Wang, L. Dai, P. Zhou, B. Lu, J. Zhou and Z. He, *Nano-Micro Letters*, 2022, **14**, 218.
31. H. Gan, J. Wu, F. Zhang, R. Li and H. Liu, *Energy Storage Materials*, 2023, **55**, 264-271.
32. H. Gan, J. Wu, R. Li, B. Huang and H. Liu, *Energy Storage Materials*, 2022, **47**, 602-610.
33. X. Zhang, J. Li, K. Qi, Y. Yang, D. Liu, T. Wang, S. Liang, B. Lu, Y. Zhu and J. Zhou, *Adv Mater*, 2022, **34**, e2205175.
34. Y. Zhang, Z. Zeng, S. Yang, Y. Zhang, Y. Ma and Z. Wang, *Energy Storage Materials*, 2023, **57**, 557-567.
35. H. Yang, R. Zhu, Y. Yang, Z. Lu, Z. Chang, P. He, C. Zhu, S. Kitano, Y. Aoki, H. Habazaki and H. Zhou, *Energy & Environmental Science*, 2023, **16**, 2133-2141.
36. Y. Zhang, Z. Zeng, S. Yang, Y. Zhang, Y. Ma and Z. Wang, *Energy Storage Materials*, 2023, DOI: <https://doi.org/10.1016/j.ensm.2023.03.001>.
37. X. Ge, W. Zhang, F. Song, B. Xie, J. Li, J. Wang, X. Wang, J. Zhao and G. Cui, *Advanced Functional Materials*, 2022, **32**.